Supplementary Information for

Investigating CO Electrolysis on cobalt at elevated temperatures to produce C_{4+} hydrocarbons

Nishithan C. Kani[a], Mohd Riyaz[b], Carolina Isabella Elizarraras[a], Emilia Wessel[a], Kasper Enemark-Rasmussen[c], Qamar Nisa[d], John Varcoe[d], Alexander Bagger[b]*, and Brian Seger[a]*

[a]Surface Physics & Catalysis (SurfCat) Section, Department of Physics, Technical University of Denmark, 2800 Kongens Lyngby, Denmark.

[b]Catalysis Theory (CatTheory) Center, Department of Physics, Technical University of Denmark, 2800 Kongens Lyngby, Denmark.

[c]Department of Chemistry, Technical University of Denmark, 2800 Kongens Lyngby, Denmark.

[d]Department of Chemistry, School of Chemistry and Chemical Engineering, University of Surrey, Guildford, GU2 7XH, UK.

Corresponding Authors:

Prof. Brian Seger, E-mail: brse@fysik.dtu.dk
Prof. Alexander Bagger, E-mail: alexbag@dtu.dk

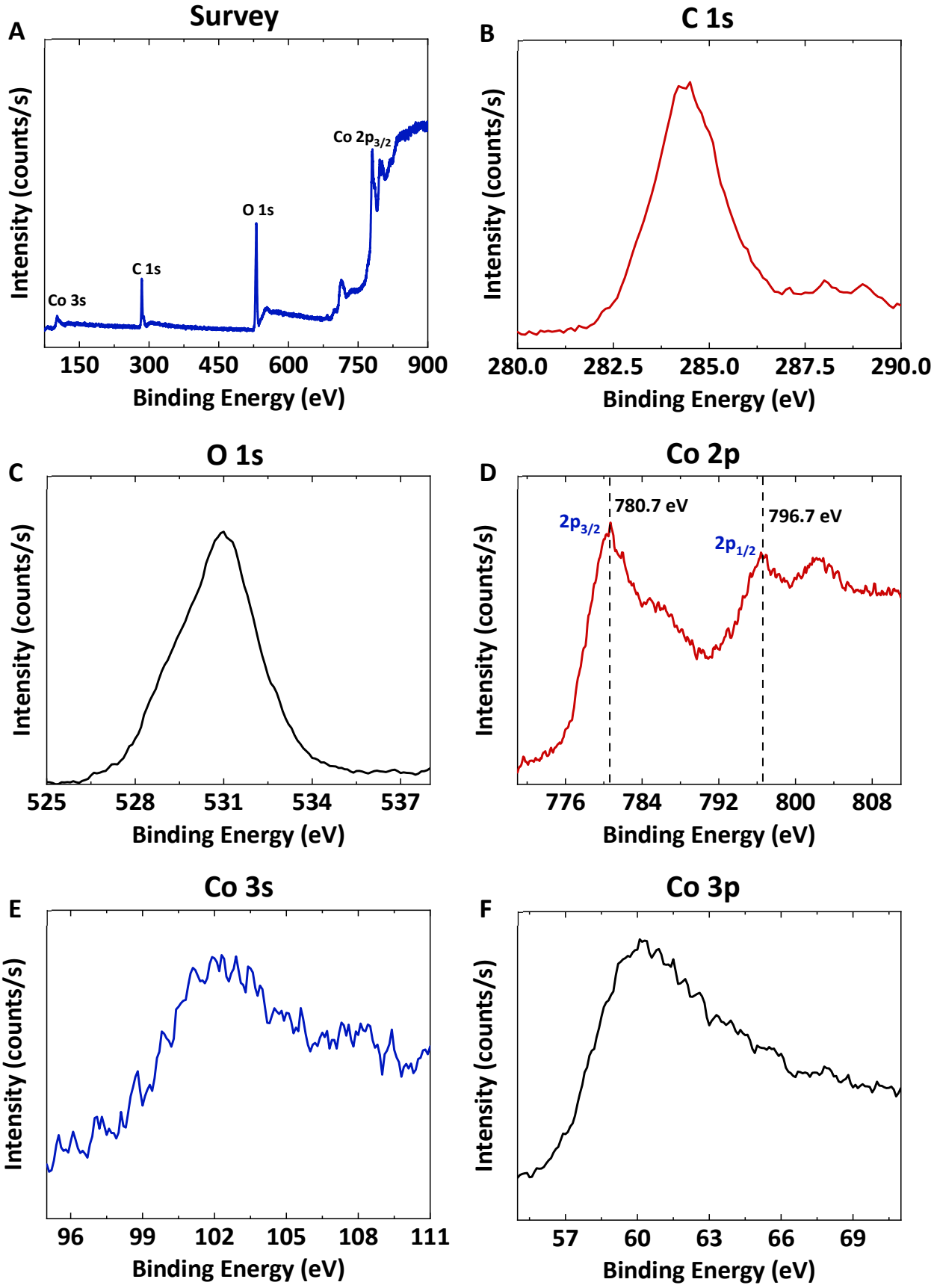

Figure S1: X-ray photo electron spectra for cobalt GDE: A) Survey scan. **High resolution scans** B) C 1s C) O 1s D) Co 2p E) Co 3s F) Co 3p.

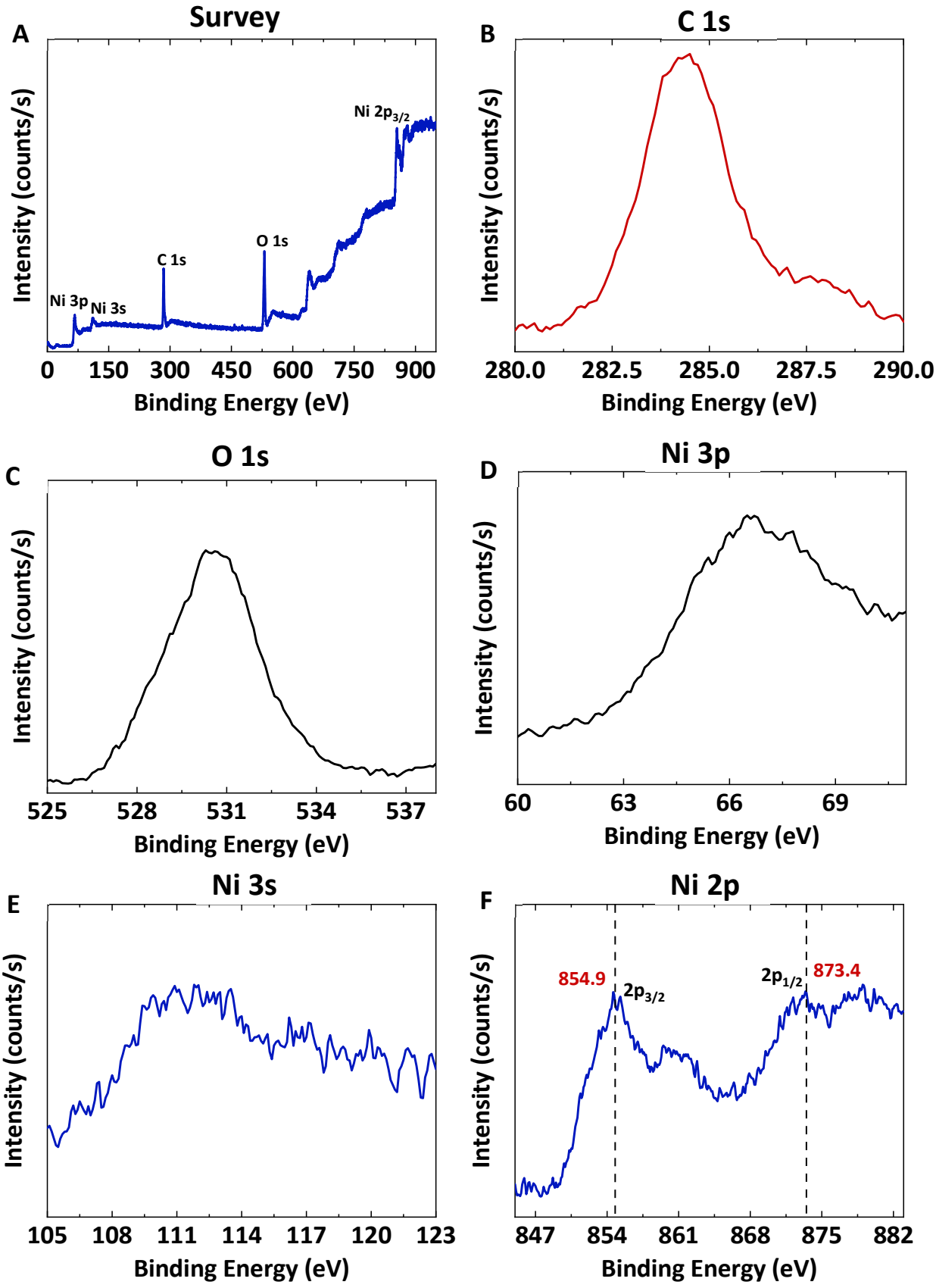

Figure S2: X-ray photoelectron spectra for Ni fiber paper anode: A) Survey scan. **High resolution scans** B) C 1s C) O 1s D) Ni 3p E) Ni 3s F) Ni 2p.

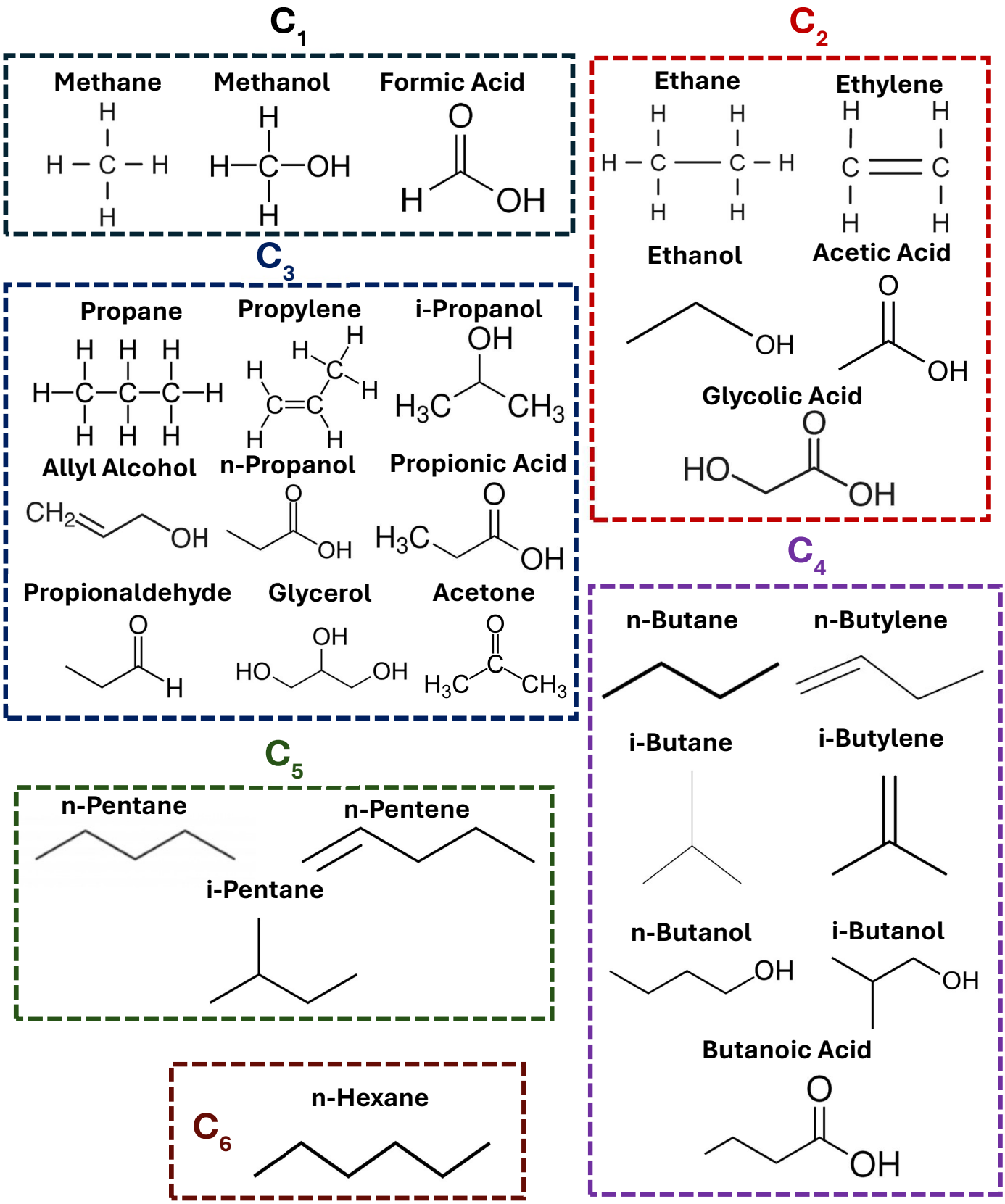

Figure S3: List of products detected from CO electrolysis on cobalt. *(Experimental Conditions: Cathode - 100 nm Co on Sigracet 39BB GDE, Anode – Ni fiber paper, Membrane – MPIP AEM, 0.1 M CsOH anolyte, MEA Cell, 80 °C, 250 mA/cm^2, 3 h.)*

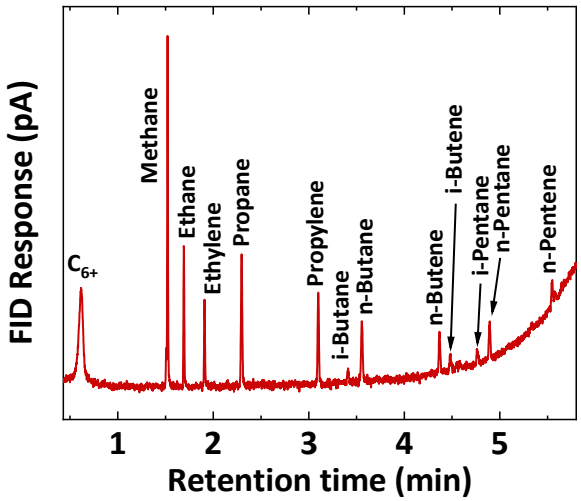

Figure S4: FID spectrum corresponding to COE electrolysis on cobalt experiments in Figure 1. *(Experimental Conditions: Cathode - 100 nm Co on Sigracet 39BB GDE, Anode – Ni fiber paper, Membrane – MPIP AEM, 0.1 M CsOH anolyte, MEA Cell, 80 ˚C, 250 mA/cm^2, 3 h.)*

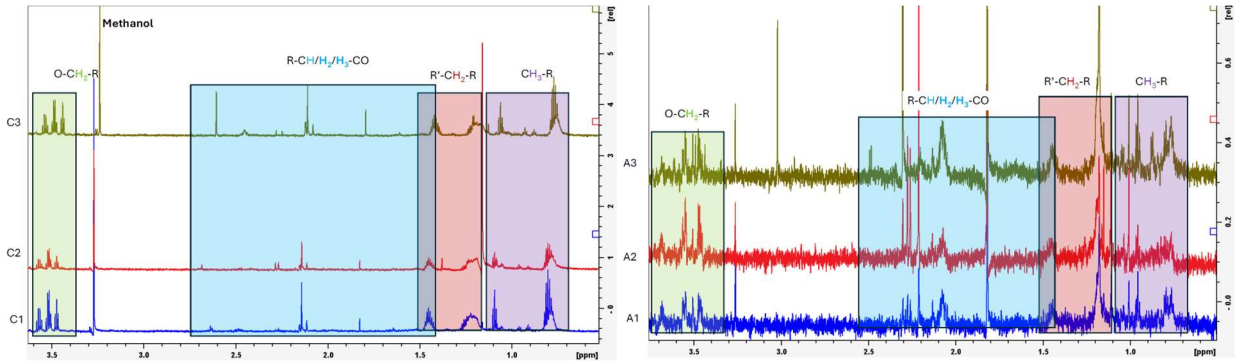

Figure S5: Representative NMR spectra of liquid samples.

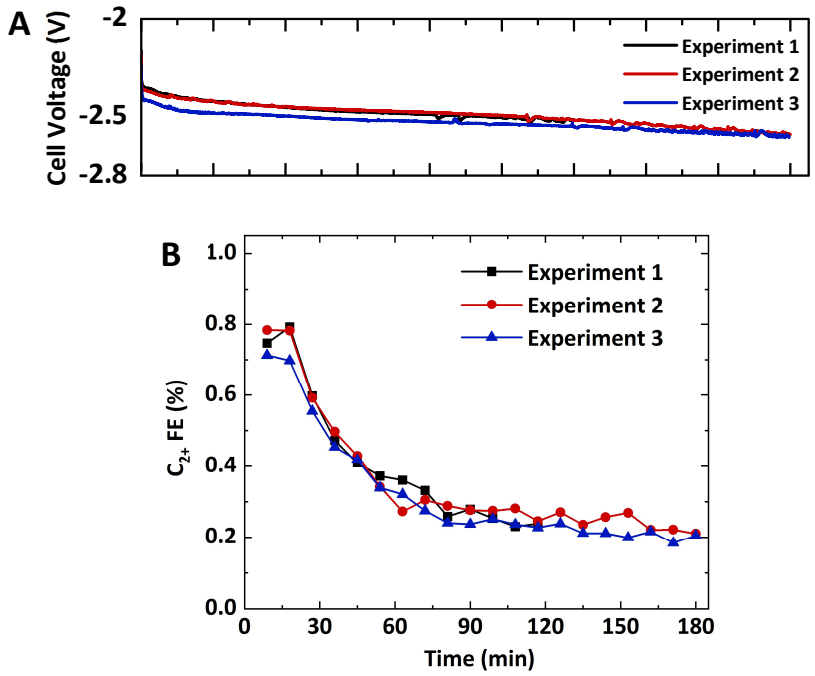

Figure S6: A) Cell voltages corresponding to Figure 1 data. B) Triplicates of the gas phase C_{2+} products FE at -250 mA/cm^2 as a function of time. *(Experimental Conditions: Cathode - 100 nm Co on Sigracet 39BB GDE, Anode – Ni fiber paper, Membrane – MPIP AEM, 0.1 M CsOH anolyte, MEA Cell, 80 °C, 250 mA/cm^2, 3 h.)*

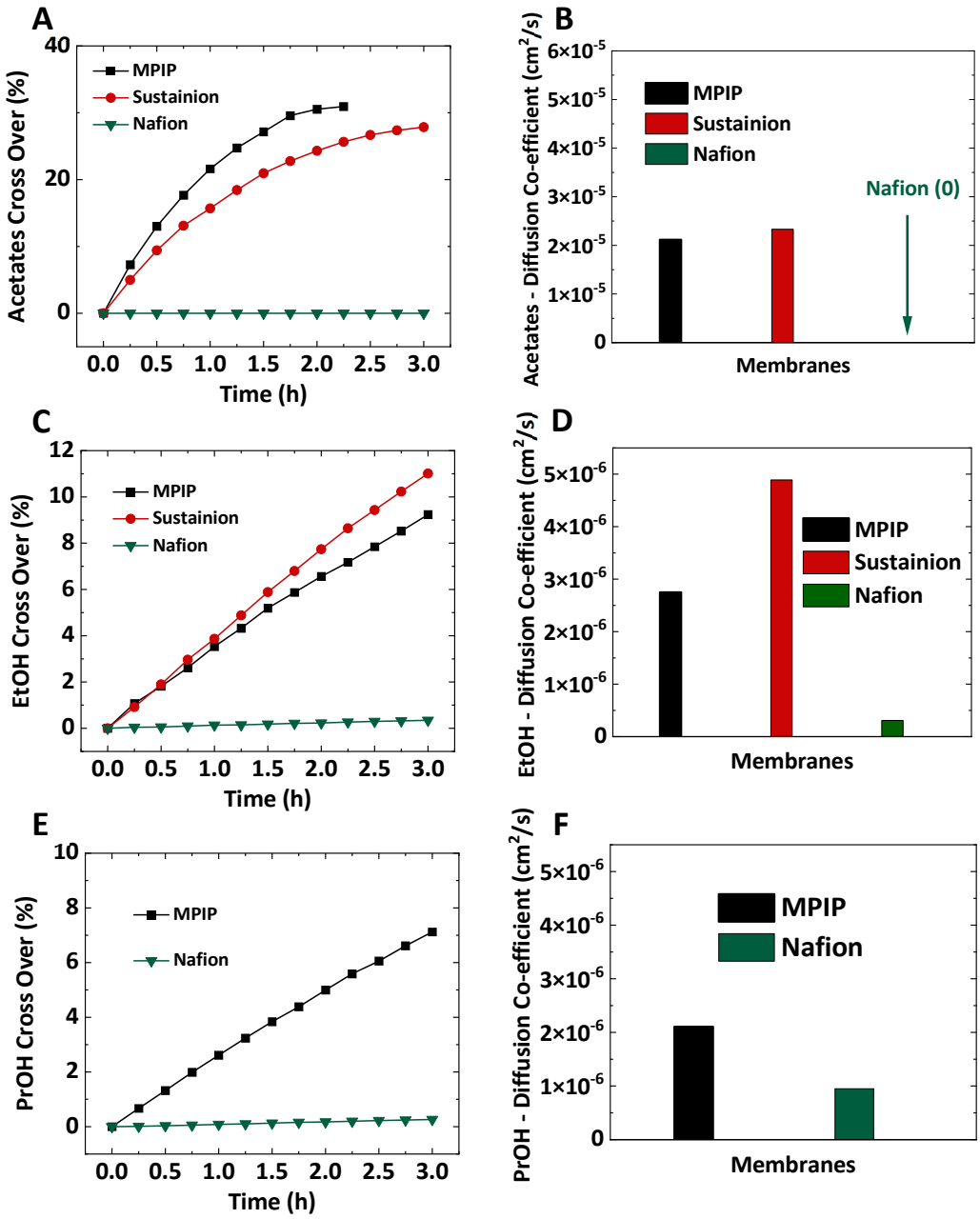

Figure S7: Crossover of products from cathode side to anode side via membranes. A) Acetates Crossover % as a function of time. B) Fitted diffusion co-efficients of acetates for different membranes. C) Ethanol Crossover % as a function of time. D) Fitted diffusion co-efficients of ethanol for different membranes. E) Propanol Crossover % as a function of time. F) Fitted diffusion co-efficients of propanol for different membranes. *(The experiments were performed in the same MEA cell but without electrodes. 0.1 M of product in 0.1 M of CsOH was flowed on the cathode side and 0.1 M CsOH was flowed on the anode side. The membrane contact area was 1 cm^2. The experiments were conducted at room temperature for a period of 3 h.)*

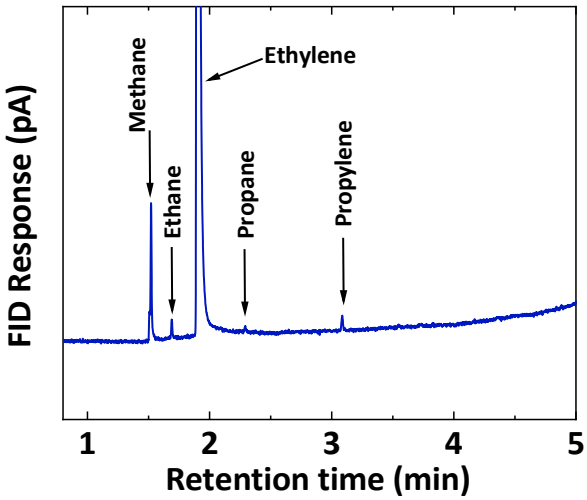

Figure S8: ***FID spectrum for CO electrolysis on Cu GDE at 80 ˚C.*** *C_{4+} products are not observed. (Experimental Conditions: Cathode – 150 nm Cu on Sigracet 39BB GDE, Anode – Ni fiber paper, Membrane – MPIP AEM, 0.1 M CsOH anolyte, MEA Cell, 80 ˚C, -250 mA/cm^2, Spectra taken at 27 min.)*

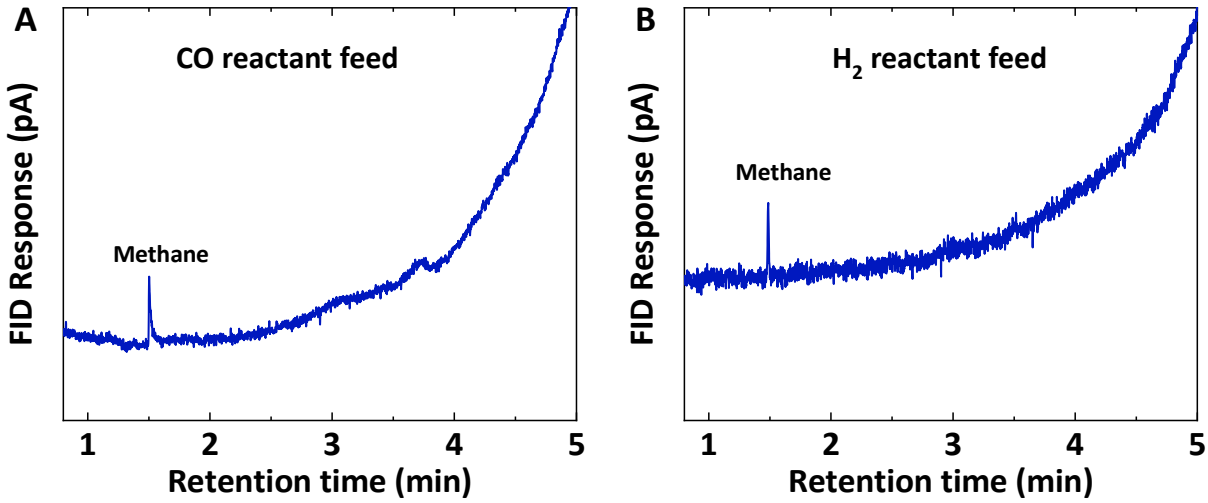

Figure S9: FID spectra for reactants. A) CO reactant. B) H_2 reactant. Only CH_4 was detected in both the cases, and no other hydrocarbons were detected. In the case of CO, 9 ppm was detected corresponding to a current density of -0.12 mA/cm^2 and in the case of H_2, 4 ppm was detected corresponding to a current density of -0.015 mA/cm^2.

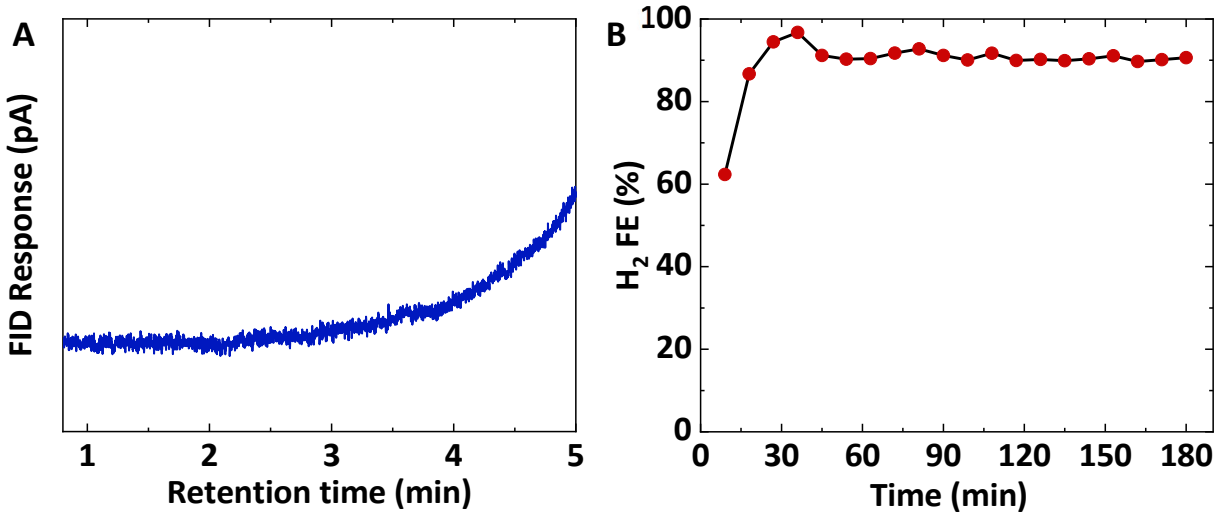

Figure S10: Ar control experiment. The CO reactant was replaced with Ar and electrolysis was conducted at 80 ˚C A) FID spectrum of the product gases. No hydrocarbons were detected. H_2 was the only detected product resulting from water electrolysis. B) H_2 Faradaic efficiency as a function of time. *(Experimental Conditions: Ar feed, Cathode - 100 nm Co on Sigracet 39BB GDE, Anode – Ni fiber paper, Membrane – MPIP AEM, 0.1 M CsOH anolyte, MEA Cell, 80 ˚C, -250 mA/cm^2, 3 h.)*

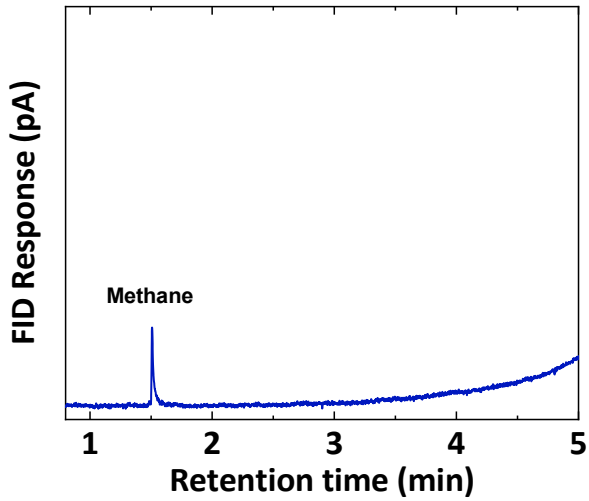

Figure S11: FID spectrum for Open circuit control experiment. CO and H_2 were sent into the MEA cell at a molar ratio of 1:2 and the temperature was maintained at 80 ˚C. No cell voltage or current density were applied. The outlet stream *was* sent to the GC for the detection of products. Only methane (20 ppm) was *detected,* and no other hydrocarbons were detected. The detected methane are contaminants from the reactants, CO and H_2 as shown in Figure S11. *(Experimental Conditions: CO:H_2 feed – 1:2, Cathode - 100 nm Co on Sigracet 39BB GDE, Anode – Ni fiber paper, Membrane – MPIP AEM, 0.1 M CsOH anolyte, MEA Cell, 80 ˚C, Open circuit, 3 h.)*

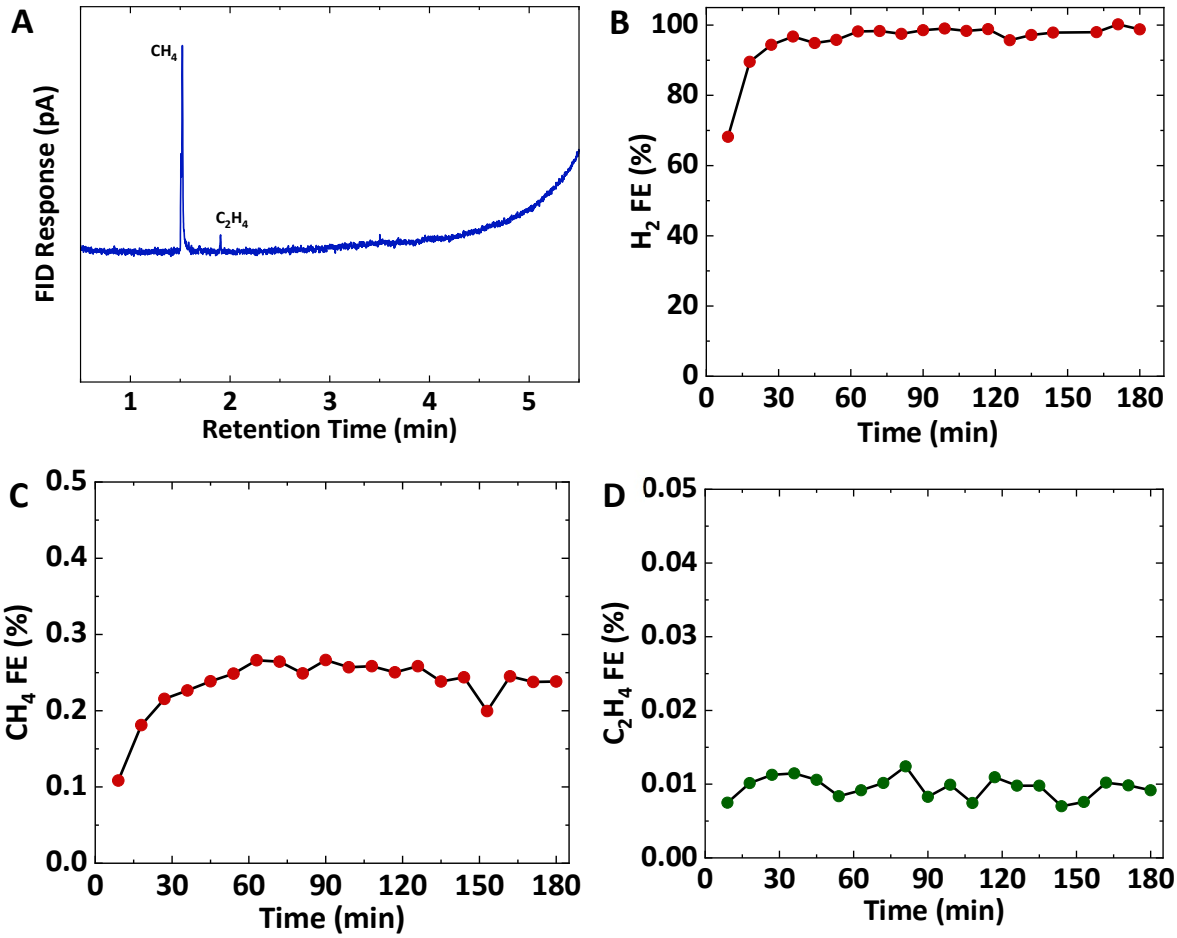

Figure S12: Blank GDE control experiment. A) FID Spectrum of the product gases. B) H_2 Faradaic efficiency as a function of time. C) CH_4 Faradaic efficiency as a function of time. D) C_2H_4 Faradaic efficiency as a function of time. No other products were detected. *(Experimental Conditions: CO reactant feed, Cathode - Blank Sigracet 39BB carbon GDE, Anode – Ni fiber paper, Membrane – MPIP AEM, 0.1 M CsOH anolyte, MEA Cell, 80 °C, -250 mA/cm^2, 3 h.)*

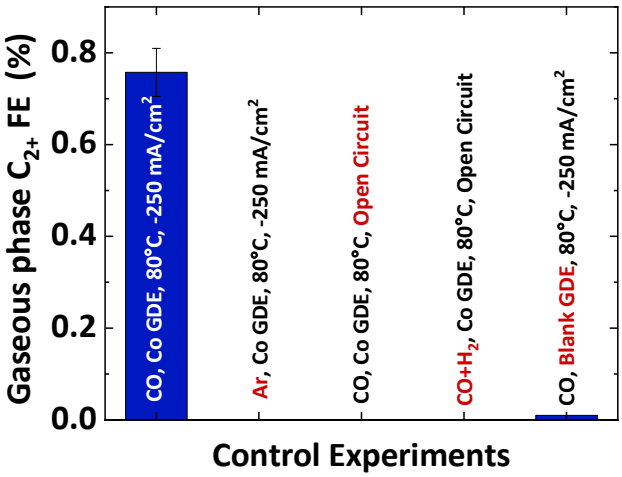

Figure S13: Control Experiments. Gas phase C_{2+} products Faradaic efficiencies for different control experiments. *(Experimental Conditions: Cathode - 100 nm Co on Sigracet 39BB GDE/ Blank Sigracet 39BB GDE, Anode – Ni fiber paper, Membrane – MPIP AEM, 0.1 M CsOH anolyte, MEA Cell, 80 ˚C, 3 h.)*

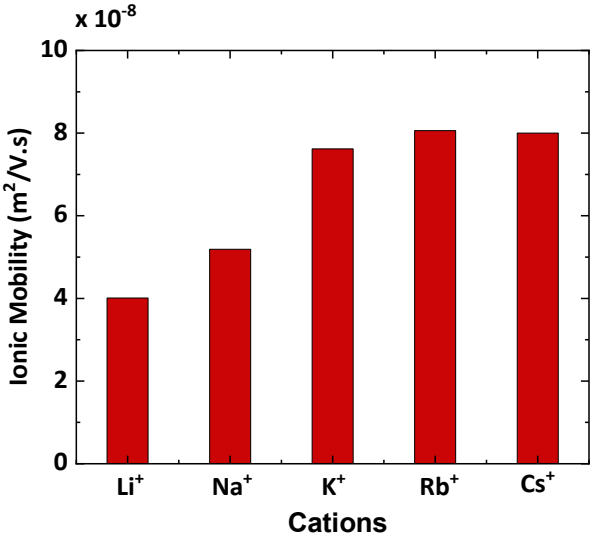

Figure S14: Ionic mobilities of different alkali metal cations. *(Data taken from CRC Handbook of Chemistry and Physics, 105th edition)*

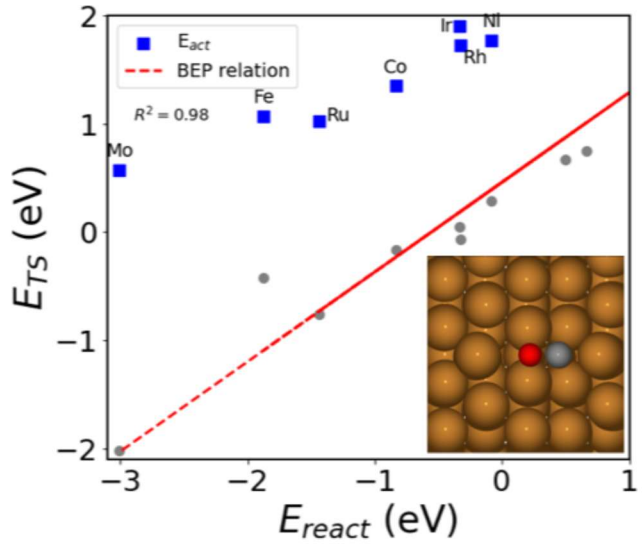

Figure S15: CO dissociation barrier on various metal surfaces, B_5-site.

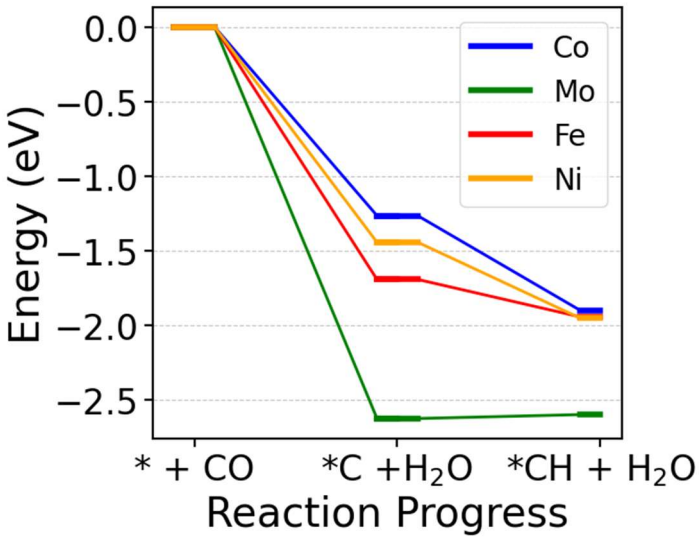

Figure S16: Comparison of E_{ads} of *C and *CH on Ni, Co, Fe, and Mo with reference to gas phase CO.

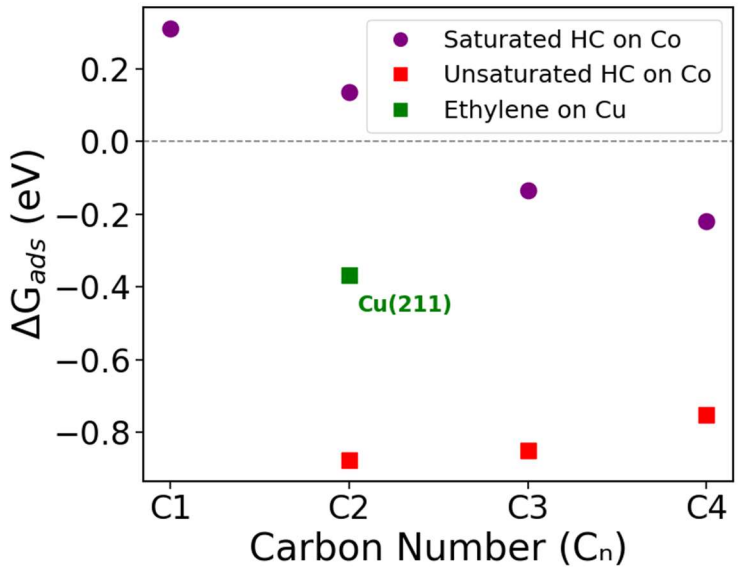

Figure S17: Free energy of adsorption for saturated and unsaturated hydrocarbons on the Co step site compared to Cu at standard conditions (p = 1 bar, T = 300 K).

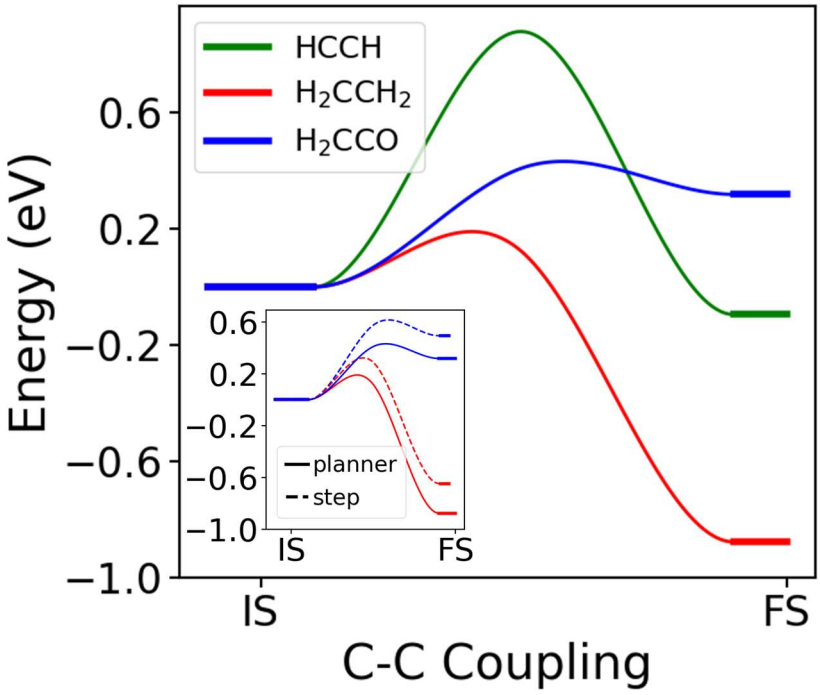

Figure S18: Kinetic barriers for different C–C coupling pathways during carbon chain growth. *CH_2-CH_2 and *CH_2-CO show low barriers, 0.12 eV and 0.41 eV, respectively. Thus, both of these steps are likely for C-C coupling at room temperature. The inset shows the difference in the C-C coupling barrier at the planar and step-edge sites.

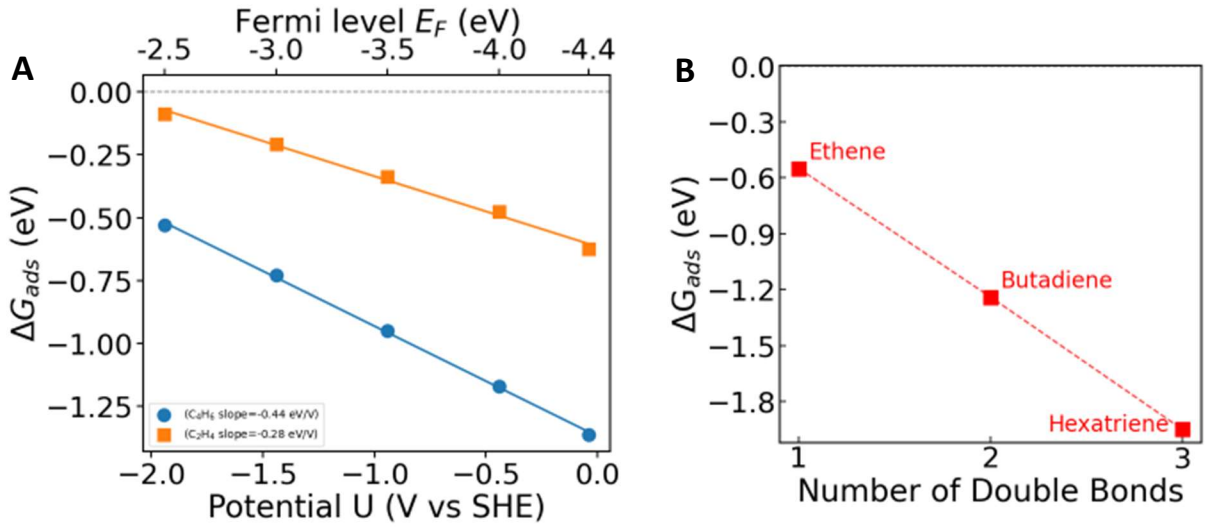

Figure S19: A) Effect of applied potential on the adsorption energies (E_{ads}) of ethylene and butadiene on the Co (0001) planar site. The adsorption energy at each potential is obtained by varying the slab reference Fermi level, E_{FERMI}^{ref}. B) Change in Adsorption energy with increase in the number of unsaturated bonds.

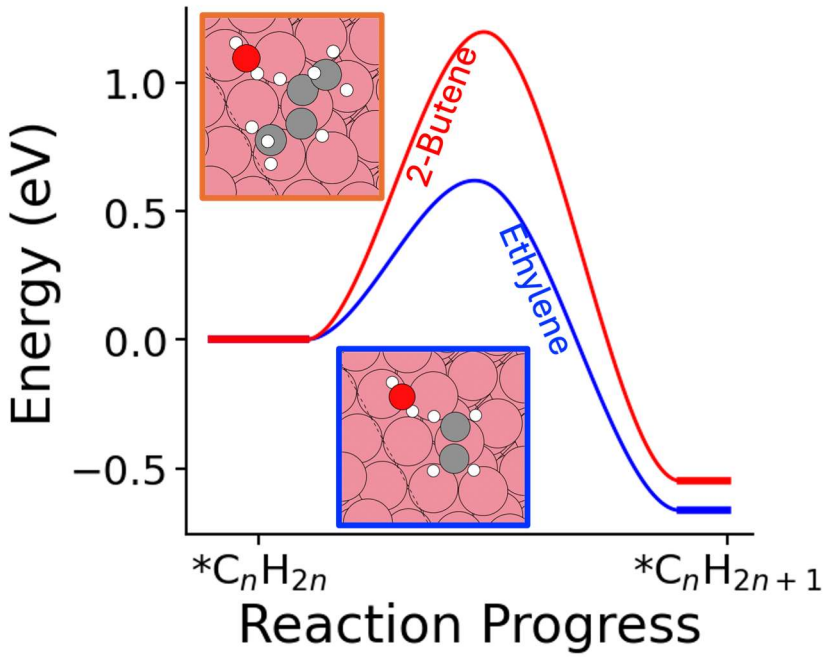

Figure S20: Kinetic barrier for hydrogenation of unsaturated primary and secondary carbon sites of the adsorbed hydrocarbon.

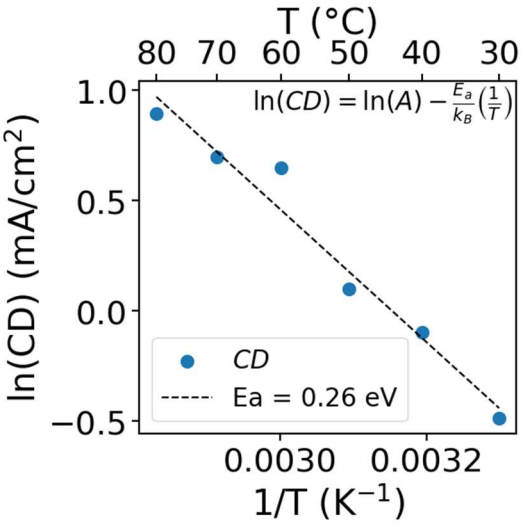

Figure S21: The apparent activation energy calculated from the Arrhenius plot of current density (CD) vs 1/T.

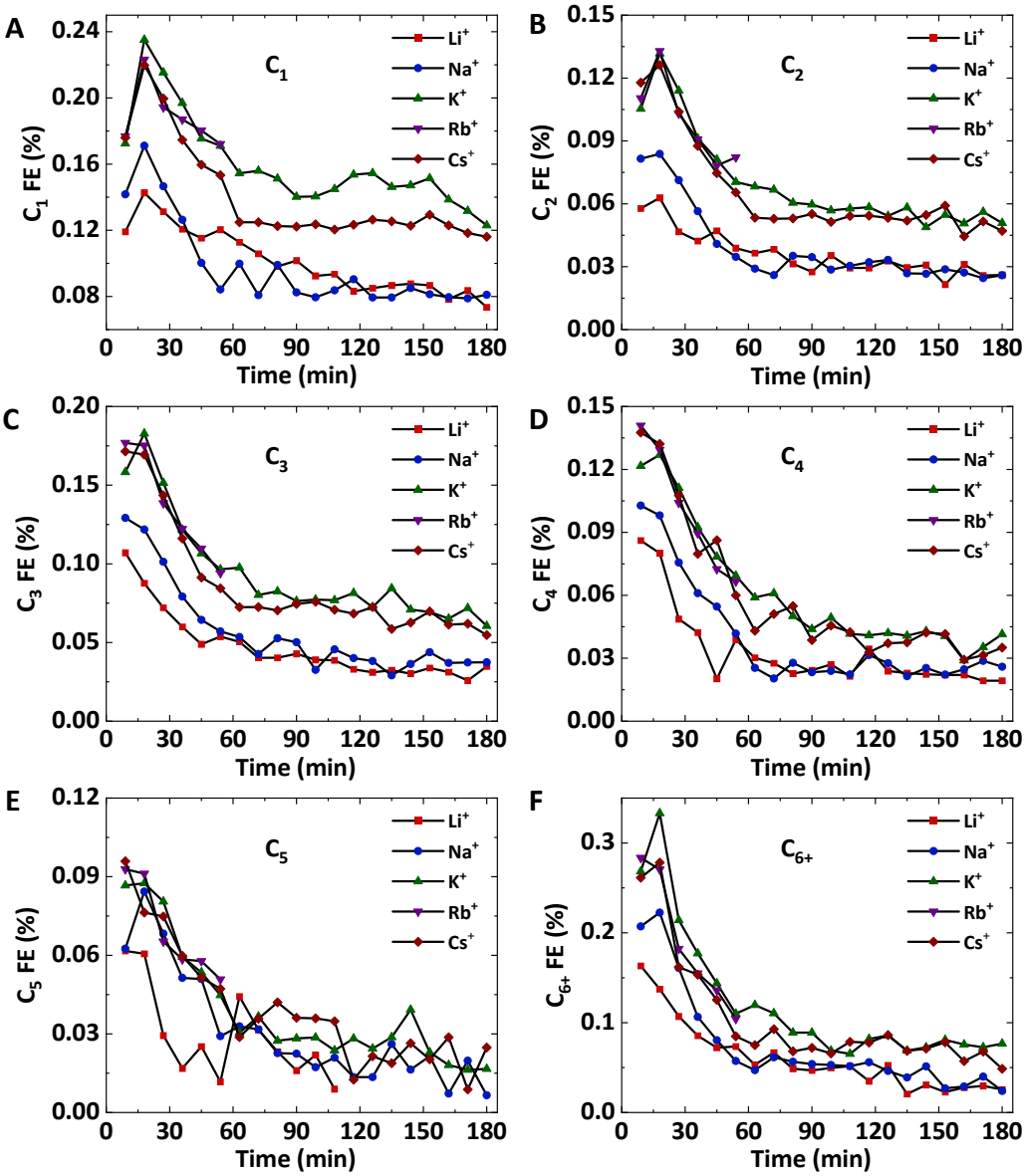

Figure S22: Gaseous products Faradaic efficiencies when the cation speciation in the anolyte is varied. A) C_1. B) C_2. C) C_3. D) C_4. E) C_5. F) C_{6+}. *(Experimental Conditions: Cathode – 10 nm Co on Sigracet 39BB GDE, Anode – Ni fiber paper, Membrane – MPIP AEM, 0.1 M MOH anolyte, M is cation being varied MEA Cell, 80 °C, -250 mA/cm^2, 3 h.)*

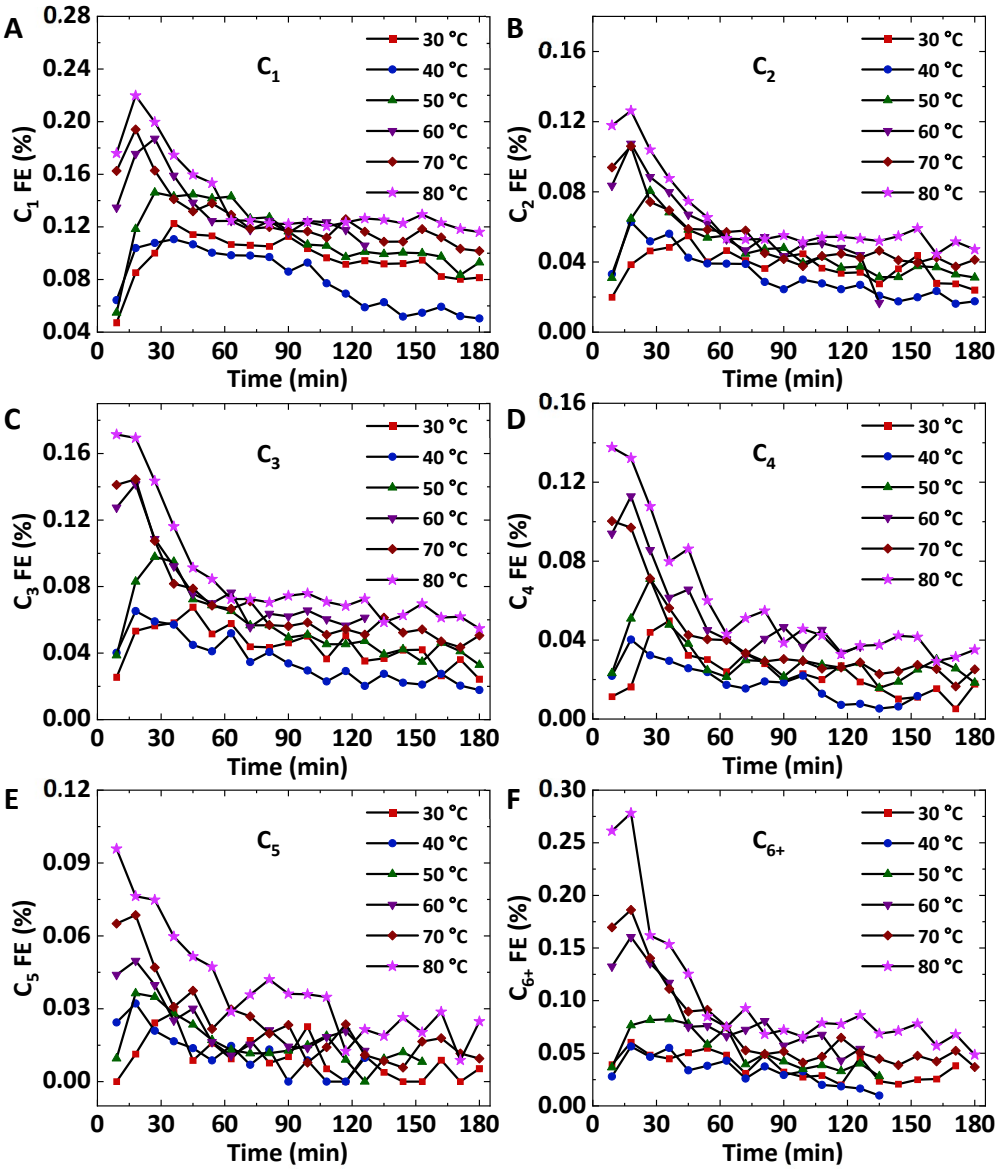

Figure S23*:* Gaseous products Faradaic efficiencies when the temperature is varied. A) C_1. B) C_2. C) C_3. D) C_4. E) C_5. F) C_{6+}. *(Experimental Conditions: Cathode – 100 nm Co on Sigracet 39BB GDE, Anode – Ni fiber paper, Membrane – MPIP AEM, 0.1 M CsOH anolyte, MEA Cell, -250 mA/cm², 3 h.)*

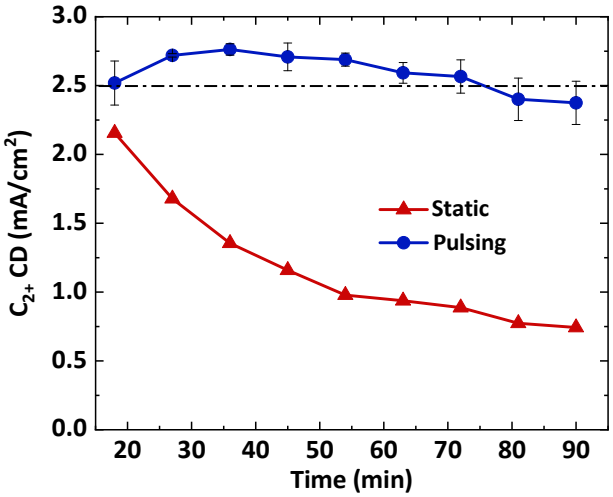

Figure S24: C_{2+} current densities (CD) for Static vs pulsed operation. Static operation: -250 mA/cm^2; Pulsed operation: -250 mA/cm^2 for 30 s and +25 mA/cm^2 for 30 s. *(Experimental Conditions: Cathode – 100 nm Co on Sigracet 39BB GDE, Anode – Ni fiber paper, Membrane – MPIP AEM, 0.1 M MOH anolyte; M varied from Li^+ to Cs^+, MEA Cell, 80 ˚C, 3 h.)*

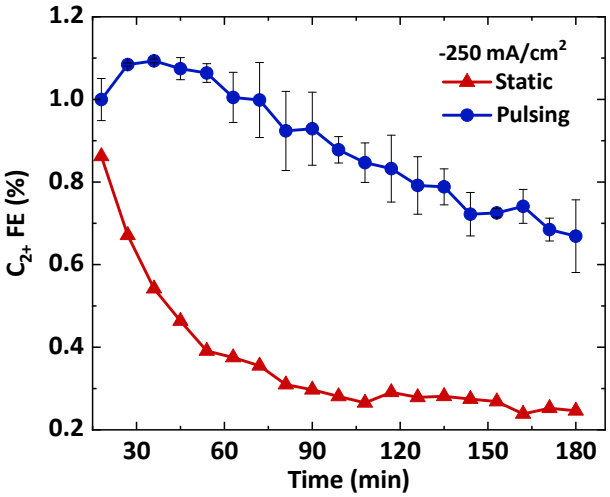

Figure S25: Investigation of catalyst stability. C_{2+} FE for Static vs pulsed operation. Static operation: -250 mA/cm^2; Pulsed operation: -250 mA/cm^2 for 30 s and +25 mA/cm^2 for 30 s. *(Experimental Conditions: Cathode – 100 nm Co on Sigracet 39BB GDE, Anode – Ni fiber paper, Membrane – MPIP AEM, 0.1 M MOH anolyte; M varied from Li^+ to Cs^+, MEA Cell, 80 ˚C, 3 h.)*

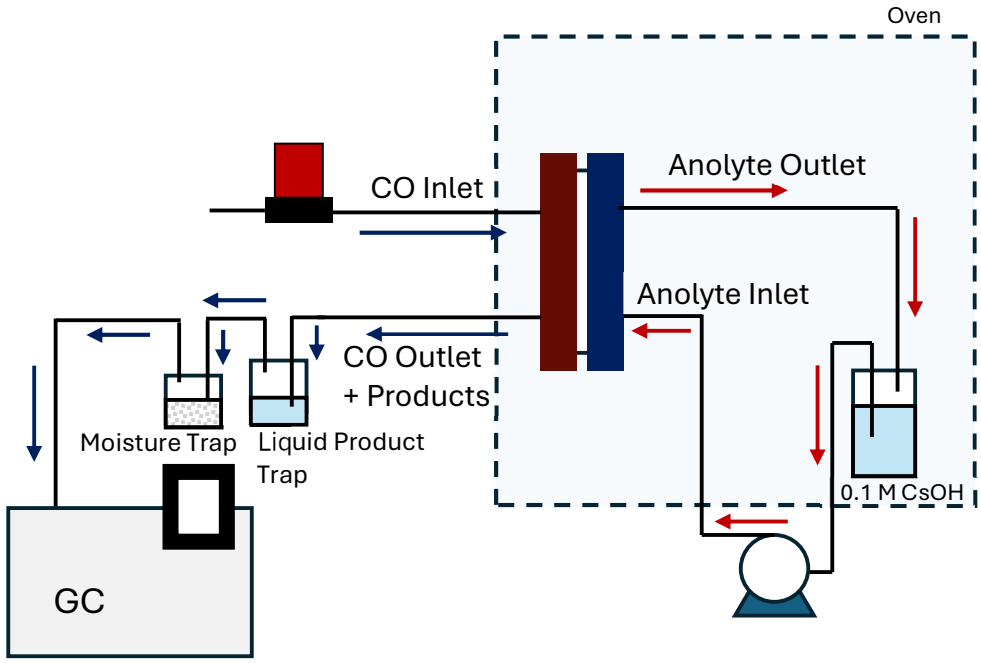

Figure S26: Schematic of the experimental setup.

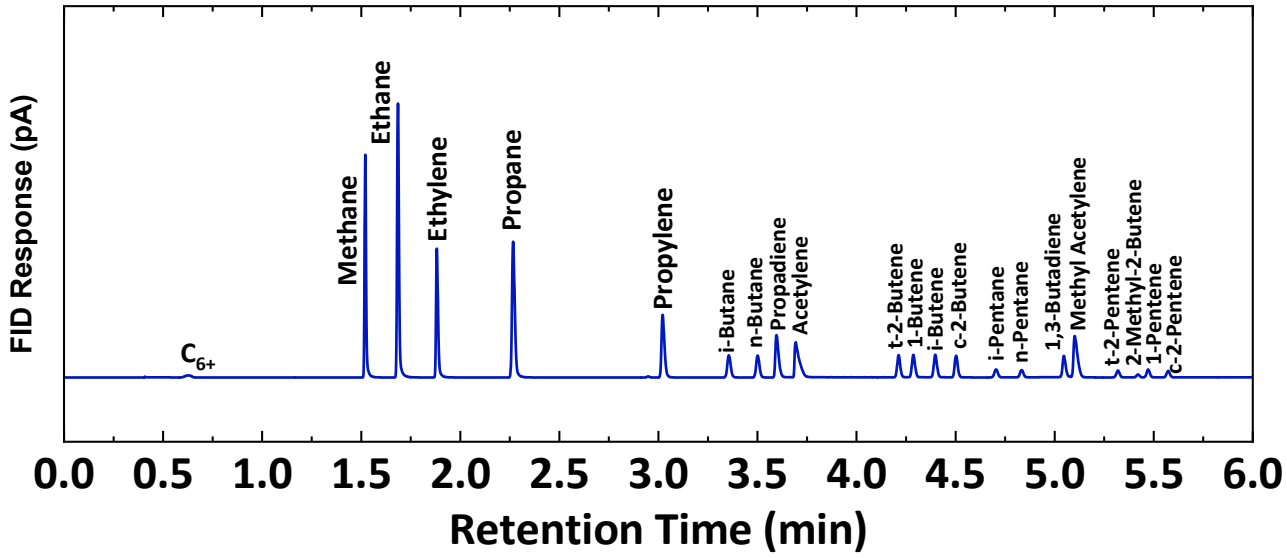

Figure S27: FID spectrum of the calibration gas sample.

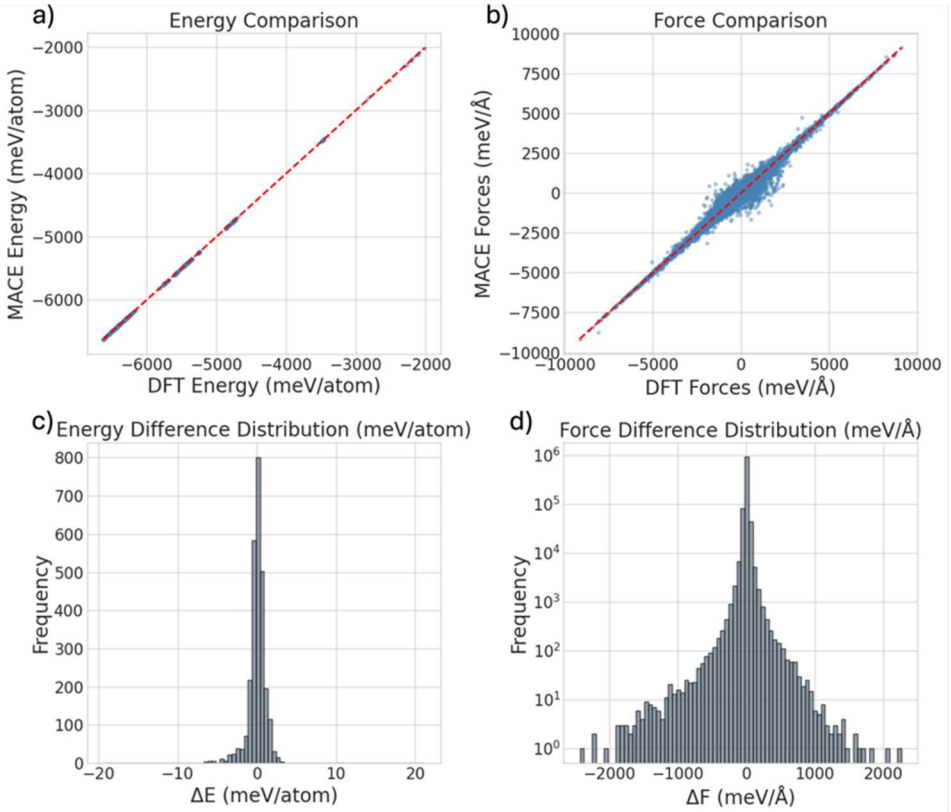

Figure S28: Comparison between DFT and MACE results on the test set. a) and (b) present parity plots for the predicted energies and forces, respectively. Panels (c) and (d) illustrate the distributions of the corresponding energy and force errors.

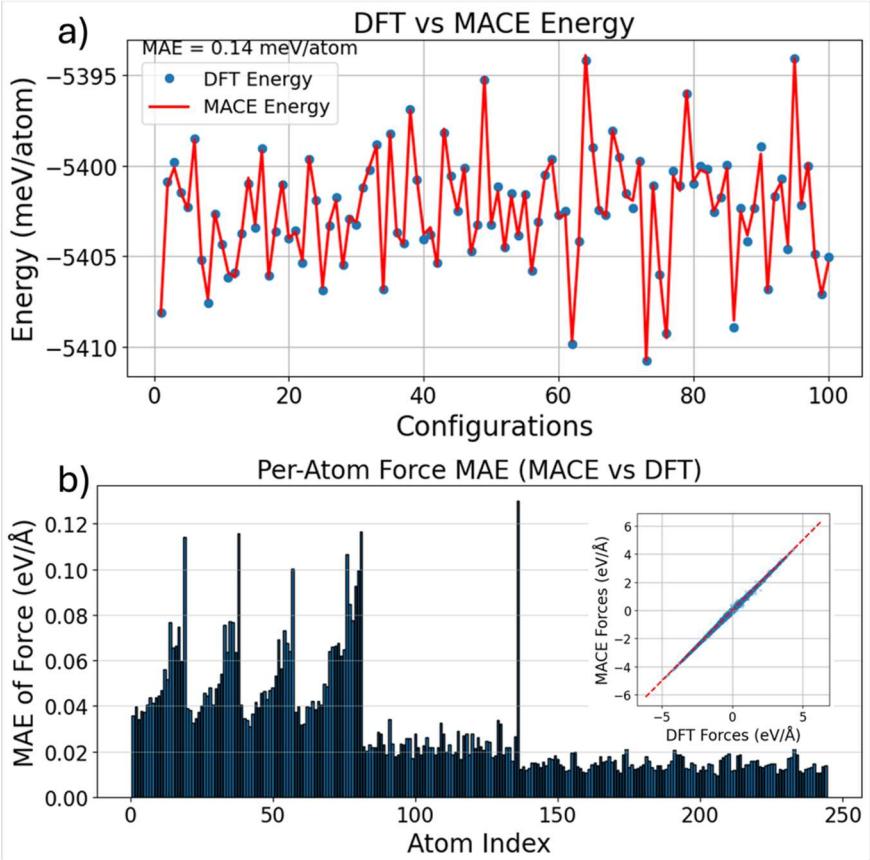

Figure S29: (a) DFT–MACE energy comparison for CO adsorbed on a Co surface in explicit solvent. (b) Force uncertainty as a function of atomic index. Both are computed over 100 meta dynamics frames near the transition state region (C–O bond length: 1.7–2.2 Å).

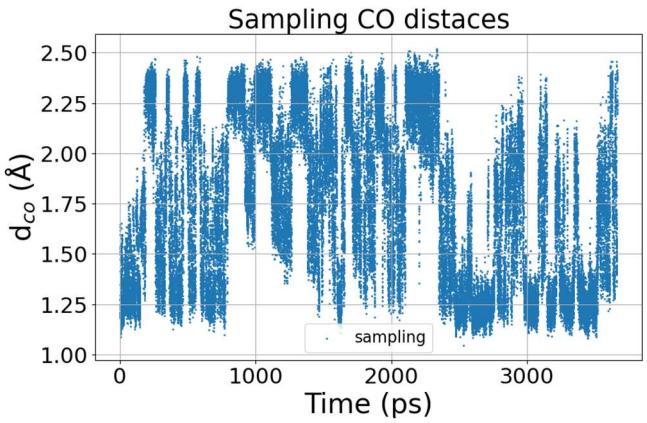

Figure S30: C-O bond distance as a function of time sampled using the OPES method. This shows how the enhanced sampling method explores different regions of the free-energy landscape during the simulation.

Sl.No.	Hydrocarbon	Boiling Point (°C)
1	Methane	-162
2	Ethane	-89
3	Ethylene	-104
4	Propane	-42
5	Propylene	-48
6	Butane	-1
7	Butene	-6
8	Pentane	36
9	Pentene	30
10	Hexane	69

Table S1: Boiling points of hydrocarbons. *(Data from CRC handbook of Physics and Chemistry, 105th edition.)*

Sl.No.	Electrolyte salts	Purity (%)	Vendor	Part number
1	LiOH	99.95	Sigma-Aldrich	254274
2	NaOH	99.99	Sigma-Aldrich	1064660050
3	KOH	99.95	Sigma-Aldrich	757551
4	RbOH	99.99	Sigma-Aldrich	401293
5	CsOH	99.95	Sigma-Aldrich	516988

Table S2: Details of the electrolyte salts used for the experiments

Supplementary Note 1 (SN1)

Anderson-Schulz-Flory (ASF) Model – Fitting Details

The chain growth probability (α) was estimated from the slope of $\ln(X_n/n)$ plotted against n, where X_n denotes the mass fraction and n represents the carbon number. The fitting was performed using the mass fractions of C_1-C_5 hydrocarbons.

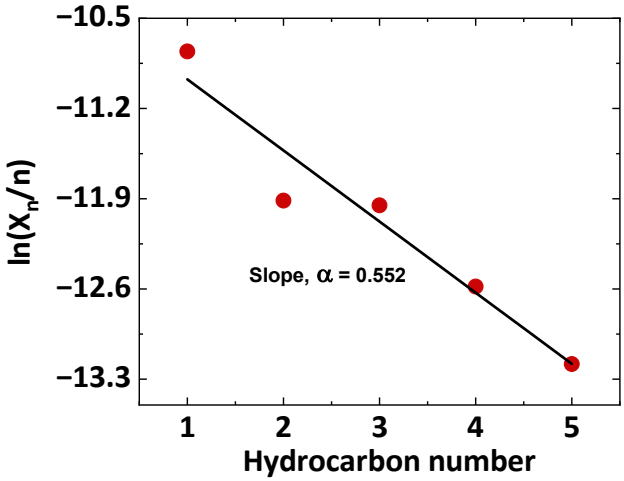

Figure S31: Anderson-Schulz-Flory (ASF) Model – Fitting. The chain growth probability (α) was estimated to be 0.552. Mass fractions of C_1 - C_5 hydrocarbons were used for the fitting.

We estimated the mass fractions of C_6 - C_{15} hydrocarbons using a recursive formula derived from the ASF chain growth probability distribution.[1]

$$X_{n+1} = X_n \left(\frac{n+1}{n}\right) \alpha$$

The estimated mass fractions were subsequently converted into partial current densities.

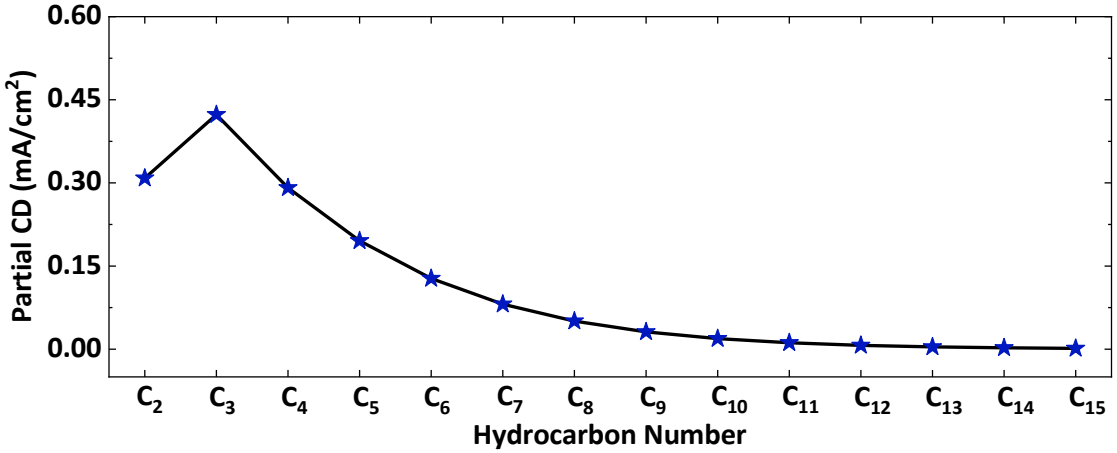

Figure S32: Estimated partial current densities for the CO electrolysis on Co based on the Anderson-Schulz-Flory (ASF) model fitted using C_1 to C_5 mass fractions. The chain growth probability, α = 0.552.

Supplementary Note 2 (SN2)

***CO dissociation vs protonation**

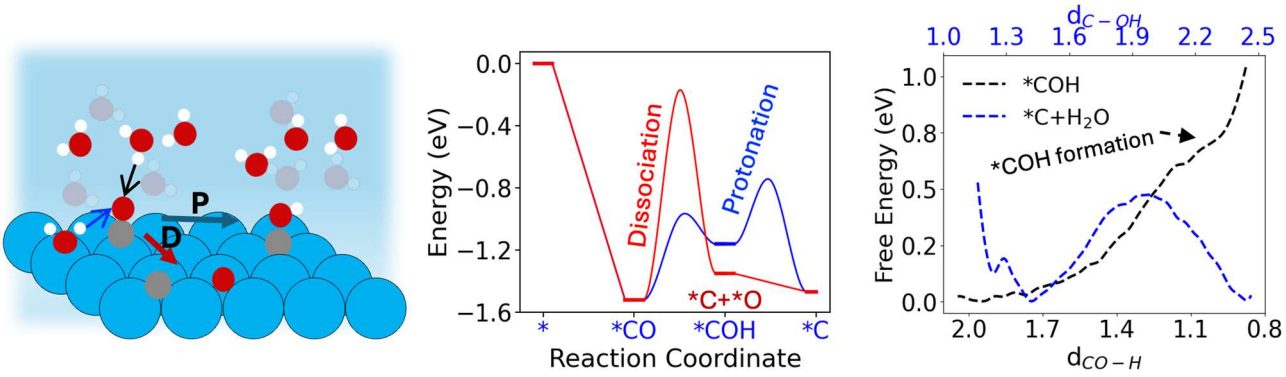

Figure S33: (a) Schematic illustration of hydrogen transfer via chemical and electrochemical pathways (blue and black arrow). P and D mean protonation and dissociation path (b) Comparison of kinetic and thermodynamic barriers for H-transfer from $*O_2H$ to *CO on Co step sites (where *C is coordinated to four Co atoms). The red curve is the CO dissociation barrier (c). 1D Free energy path for electrochemical hydrogen transfer from solution-phase H_2O to *CO (black) and *COH (blue) forming *C and H_2O.

Understanding of proton-transfer processes in an electrochemical process presents several challenges, including the need to maintain constant potential during charge transfer, the disparity in time scales between solvent reorientation, proton transfer, and electron transfer. Here, we evaluated the proton-transfer barrier using two complementary approaches. In the first approach, a static DFT calculation was performed for the adsorbed phase, where a hydrogen atom is transferred from an adsorbed H_2O molecule to CO, forming *OH and *CO species on the surface. Previous Janik el al.[2] showed that this adsorbed-phase barrier can approximate the electrochemical proton-transfer barrier at the potential where *OH and OH^- are in equilibrium. In the second approach, we employed the OPES_META enhanced sampling method to calculate the proton-transfer barrier from solvated H_2O, leading to the formation of *COH and OH^- in the solution phase. A schematic representation of these processes, along with direct CO dissociation, is shown in **Figure S33A**, and the corresponding energy profiles are presented in **Figure S33B** and **Figure S33C**. The solution-phase protonation barrier is considerably higher than the adsorbed-phase barrier due to the intrinsic instability of OH^- in the absence of an applied potential. Since this step is potential-dependent, the barrier height is expected to decrease under reducing conditions, with an approximate slope of one. The computed energetics reveal that the protonation barrier is lower than the CO dissociation barrier, suggesting that protonation is the energetically preferred pathway under electrochemical conditions.

Supplementary Note 3 (SN3)

MEA Cell Assembly: The MEA electrolyzer was assembled beginning from the anode side. The cell bolts were inserted into the anode flow field and laid flat on a bench for alignment. A 1 cm^2 Ni fiber paper anode was then positioned at the geometric center of the anode flow field. A 0.015”-thick PTFE gasket featuring a 1 cm^2 central window was placed over the anode to define the active area and provide sealing. Next, the 3 cm^2 anion-exchange membrane (MPIP-AEM) was carefully placed on top of the gasket/anode stack, ensuring that the membrane fully covered the 1 cm^2 window and that no wrinkles or trapped

particulates were present at the sealing interface. A second PTFE gasket (0.01" thick, 1 cm^2 central window) was then placed over the membrane to complete the anode-side sealing and maintain the defined active area. The Co GDE cathode was subsequently positioned on the membrane with the catalyst-coated side facing toward (in direct contact with) the membrane. Finally, the cathode-side flow field was placed on top, and the assembly was secured by tightening nuts onto the bolts in a uniform, crosswise sequence to promote compression. The cell was then torqued in two steps using a torque wrench: first to 2 N.m and subsequently to 4 N.m to achieve the final sealing and interfacial contact pressure.

References

(1) Henrici-Olivé, G.; Olivé, S. The Fischer-Tropsch Synthesis: Molecular Weight Distribution of Primary Products and Reaction Mechanism. *Angewandte Chemie International Edition in English* **1976**, *15* (3), 136–141. https://doi.org/https://doi.org/10.1002/anie.197601361.

(2) Akhade, S. A.; Bernstein, N. J.; Esopi, M. R.; Regula, M. J.; Janik, M. J. A Simple Method to Approximate Electrode Potential-Dependent Activation Energies Using Density Functional Theory. *Catal. Today* **2017**, *288*, 63–73. https://doi.org/https://doi.org/10.1016/j.cattod.2017.01.050.